

Constraining Neutrino–Nucleon Form Factors with Charged-Current Scattering at the Electron-Ion Collider

Guang Yang¹ and Praveen Kumar^{1,2}

¹*Brookhaven National Laboratory, Upton, NY 11973, USA*

²*University of Alabama, Tuscaloosa, AL 35487, USA*

(Dated: March 3, 2026)

Next-generation neutrino oscillation experiments such as DUNE require percent-level knowledge of neutrino–nucleon interaction cross sections. The nucleon axial form factor $F_A(Q^2)$, parameterized by the axial mass M_A , is the dominant source of uncertainty in the quasi-elastic channel, and the parity-violating structure function xF_3 is poorly constrained on free nucleons. We propose using charged-current (CC) electron–proton scattering at the Electron-Ion Collider (EIC) to address both problems simultaneously. The measurement exploits three key features of the EIC: (1) helicity-selective electron bunches provide *in situ* electromagnetic background rejection; (2) a longitudinally polarized proton target enables extraction of $F_A(Q^2)$ through the target-spin asymmetry A_{UL} ; and (3) the y -distribution leverage in CC deep inelastic scattering separates F_2 and xF_3 on a *free proton*, without nuclear corrections. Using a Fisher-information analysis at $\sqrt{s} = 141$ GeV with 500 fb^{-1} of integrated luminosity, we project the Cramér–Rao statistical floor of $\delta M_A \approx 0.03$ GeV (3%). Incorporating first-order realistic detector effects: ZDC acceptance, Q^2 smearing (5%), and background noise from helicity subtraction, the projected sensitivity is severely background-limited due to the small signal-to-background ratio ($S/B \approx 3 \times 10^{-4}$) in the elastic channel. Achieving competitive sensitivity ($\delta M_A \approx 0.14$ GeV) would require $\sim 10^{-7}$ background suppression, three orders of magnitude beyond current projections. The CC DIS y -distribution provides sub-percent extraction of $xF_3^{W^-}$ over $0.05 < x < 0.5$, representing the most robust electroweak measurement in the near term.

I. INTRODUCTION

The Deep Underground Neutrino Experiment (DUNE) [19] aims to measure the CP-violating phase δ_{CP} in the neutrino mixing matrix with a precision of $\sim 5^\circ$, determine the neutrino mass ordering at $> 5\sigma$, and search for proton decay and supernova neutrinos. Achieving these physics goals requires knowledge of neutrino–nucleus interaction cross sections at the few-percent level [20]. At the relevant energies ($E_\nu \sim 1\text{--}5$ GeV), an important interaction channel is charged-current quasi-elastic (CCQE) scattering:

$$\nu_\mu + n \rightarrow \mu^- + p. \quad (1)$$

The CCQE cross section is governed by four nucleon form factors: the vector Dirac (F_1) and Pauli (F_2) form factors, the axial form factor F_A , and the pseudoscalar form factor F_P . Through the conserved vector current (CVC) hypothesis, F_1 and F_2 are constrained to a few percent precision from decades of electron–nucleon elastic scattering [30]. The pseudoscalar F_P is related to F_A by the partially conserved axial current (PCAC) relation and contributes proportionally to m_ℓ^2/M^2 , which is negligible for electrons ($\sim 10^{-7}$) and small for muons ($\sim 1\%$). The least precisely constrained ingredient is the *axial form factor* $F_A(Q^2)$.

A. The axial mass anomaly

The standard parameterization of F_A is the dipole form:

$$F_A(Q^2) = \frac{g_A}{(1 + Q^2/M_A^2)^2}, \quad (2)$$

where $g_A = F_A(0) = 1.2723 \pm 0.0023$ is precisely known from neutron beta decay [21], and M_A is the *axial mass* that controls the Q^2 dependence. The axial charge radius is $\langle r_A^2 \rangle = 12/M_A^2$.

Measurements of M_A have yielded conflicting results (Fig. 1):

- *Deuterium bubble chambers* (1970s–80s): $M_A = 1.026 \pm 0.021$ GeV [22], from quasi-free nucleon targets with minimal nuclear corrections.
- *MiniBooNE* (2010): $M_A = 1.35 \pm 0.17$ GeV on carbon [23], a $\sim 2\sigma$ excess over the world average.
- *MINERvA* (2023): The first measurement on hydrogen [24], but with limited statistics and reliance on flux modeling.

The discrepancy between the bubble chamber and MiniBooNE values, often called the “ M_A anomaly,” has been attributed to nuclear effects in carbon (multi-nucleon correlations, meson exchange currents, random phase approximation corrections) [25, 26], but the situation remains unresolved. A high-precision measurement of M_A on a *free proton* would definitively establish the nucleon-level form factor and disentangle it from nuclear effects.

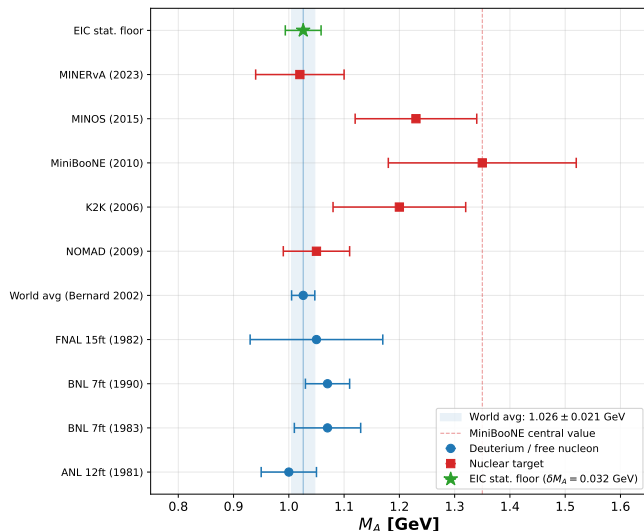


FIG. 1. Published measurements of the nucleon axial mass M_A (data compiled from Refs. [20, 22]). Blue circles: measurements on deuterium (quasi-free nucleon). Red squares: measurements on nuclear targets. Green star: EIC statistical floor ($\delta M_A = 0.032$ GeV; see Table IV). The light blue band shows the world average $M_A = 1.026 \pm 0.021$ GeV [22]; the dashed red line marks the MiniBooNE central value [23].

B. The EIC opportunity

The Electron-Ion Collider [27], under construction at Brookhaven National Laboratory, will collide longitudinally polarized electrons ($E_e = 5\text{--}18$ GeV) with longitudinally polarized protons ($E_p = 41\text{--}275$ GeV). At the maximum energy configuration (18 GeV \times 275 GeV), the center-of-mass energy is $\sqrt{s} = 141$ GeV, with a design luminosity of $\mathcal{L} = 10^{34}$ cm $^{-2}$ s $^{-1}$.

As pointed out by Klest [28], the EIC can access charged-current elastic scattering:

$$e^- + p \rightarrow \nu_e + n, \quad (3)$$

which is related to the neutrino CCQE process (1) by crossing symmetry. The key advantage is that the EIC provides a *free proton target* with *controlled beam properties*: known energy, polarization, and luminosity, none of which are available in neutrino experiments.

In this paper, we propose a three-phase measurement program:

- Phase 1: Helicity filtering** (Sec. V). Using right-handed (RH) electron bunches as an *in situ* electromagnetic background template.
- Phase 2: Axial form factor extraction** (Sec. VI). Measuring the Q^2 -binned cross section and target-spin asymmetry A_{UL} to determine M_A .
- Phase 3: Structure function extraction** (Sec. VII). Using the CC DIS y -distribution to separate $F_2^{W^-}$ and $xF_3^{W^-}$ on a free proton.

We quantify projected sensitivities using the Fisher information formalism [33], which gives the Cramér–Rao lower bound on parameter uncertainties. For the ideal projection, detector resolution, reconstruction efficiencies, and systematic uncertainties are not included; these results represent the statistical floor of the measurement. A realistic projection incorporating first-order detector effects is also presented. The purpose is to establish whether the EIC has sufficient statistical reach to make a competitive measurement, not to perform a full experimental analysis.

C. Outline

Section II reviews the theoretical framework. Section III describes the EIC experimental setup. Section IV presents the sensitivity projection methodology, including all assumptions. Sections V–VII present the three analysis phases and their results. Section VIII discusses systematics, nuclear targets, and comparisons with neutrino experiments. Section IX summarizes the conclusions.

II. THEORETICAL FRAMEWORK

A. Charged-current elastic scattering

The matrix element for the CC elastic process $e^-(k) + p(P) \rightarrow \nu_e(k') + n(P')$ is:

$$\mathcal{M} = \frac{G_F V_{ud}}{\sqrt{2}} \bar{u}(k') \gamma^\mu (1 - \gamma_5) u(k) \bar{u}(P') \Gamma_\mu u(P), \quad (4)$$

where the hadronic vertex function is:

$$\Gamma_\mu = \gamma_\mu F_1(Q^2) + \frac{i\sigma_{\mu\nu} q^\nu}{2M} F_2(Q^2) + \gamma_\mu \gamma_5 F_A(Q^2) + \frac{q_\mu}{M} \gamma_5 F_P(Q^2). \quad (5)$$

Here $q = k - k' = P' - P$ is the four-momentum transfer, $Q^2 = -q^2 > 0$, and $M = (M_p + M_n)/2 = 0.939$ GeV is the average nucleon mass.

1. Form factors

The *vector form factors* F_1 and F_2 are determined by CVC:

$$F_{1,2}^V(Q^2) = F_{1,2}^p(Q^2) - F_{1,2}^n(Q^2). \quad (6)$$

These are expressed in terms of the Sachs form factors via

$$F_1 = \frac{G_E^V + \tau G_M^V}{1 + \tau}, \quad F_2 = \frac{G_M^V - G_E^V}{1 + \tau}, \quad (7)$$

where $\tau = Q^2/(4M^2)$. We use the standard dipole parameterization for the proton,

$$G_E^p = G_D \equiv \frac{1}{(1 + Q^2/M_V^2)^2}, \quad G_M^p = \mu_p G_D, \quad (8)$$

with $M_V^2 = 0.71 \text{ GeV}^2$ and $\mu_p = 2.793$ [21], the Galster parameterization for the neutron,

$$G_E^n = -\frac{\mu_n \tau}{1 + 5.6 \tau} G_D, \quad (9)$$

and dipole scaling $G_M^n = \mu_n G_D$ with $\mu_n = -1.913$ [21]. These are known to 1–2% precision [30] and are treated as fixed inputs throughout this analysis.

The *axial form factor* $F_A(Q^2)$ is given by Eq. (2), with the two free parameters g_A and M_A . The *pseudoscalar form factor* follows from PCAC (pion-pole dominance):

$$F_P(Q^2) = \frac{2M^2 F_A(Q^2)}{Q^2 + m_\pi^2}. \quad (10)$$

For massless leptons, F_P contributes proportional to m_l^2/M^2 and is negligible.

2. Llewellyn Smith formula

The unpolarized differential cross section is [29]:

$$\frac{d\sigma}{dQ^2} = \frac{M^2 G_F^2 |V_{ud}|^2}{8\pi E_\nu^2} \left[A - B \frac{s-u}{M^2} + C \frac{(s-u)^2}{M^4} \right], \quad (11)$$

where $E_\nu = (s - M^2)/(2M)$ is the equivalent neutrino energy in the target rest frame and $s - u = 4ME_\nu - Q^2$. The minus sign before B corresponds to W^- exchange (antineutrino sign convention). The coefficients in the massless-lepton limit are:

$$A = \frac{Q^2}{M^2} [(1+\tau)F_A^2 - (1-\tau)F_1^2 + \tau(1-\tau)F_2^2 + 4\tau F_1 F_2], \quad (12)$$

$$B = \frac{Q^2}{M^2} F_A(F_1 + F_2), \quad (13)$$

$$C = \frac{1}{4} (F_A^2 + F_1^2 + \tau F_2^2). \quad (14)$$

We emphasize that the *only unknowns* in Eq. (11) are g_A and M_A , since F_1 and F_2 are fixed by CVC and F_P is negligible. The total cross section at EIC energies is $\sigma_{\text{el}} \approx 9.3 \text{ fb}$ for $M_A = 1.026 \text{ GeV}$.

3. Target-spin asymmetry A_{UL}

With a longitudinally polarized proton target, the target-spin asymmetry is:

$$A_{UL}(Q^2) = \frac{d\sigma(\uparrow) - d\sigma(\downarrow)}{d\sigma(\uparrow) + d\sigma(\downarrow)}, \quad (15)$$

where \uparrow/\downarrow denotes proton spin aligned/anti-aligned with the beam. A_{UL} arises from V–A interference and depends on the relative magnitudes of F_A and the vector form factors. At $Q^2 \rightarrow 0$, the axial coupling dominates and $|A_{UL}| \rightarrow 1$. At larger Q^2 , the vector contribution grows and the asymmetry decreases; the rate of decrease depends on M_A . We compute A_{UL} numerically using the Dirac trace technique (Appendix A).

4. Crossing symmetry

The EIC process (3) is related to the neutrino CCQE process (1) by crossing symmetry. Both probe the *same* hadronic vertex (5) with the *same* form factors. The cross sections differ only in kinematics and in the sign of the B coefficient. A measurement of M_A at the EIC therefore directly constrains the neutrino CCQE cross section.

B. CC deep inelastic scattering

At $x < 1$, the electron scatters off individual quarks inside the proton. The CC DIS cross section is:

$$\frac{d^2\sigma^{\text{CC}}}{dx dy} = \frac{G_F^2 s}{4\pi} \left(\frac{M_W^2}{Q^2 + M_W^2} \right)^2 [Y_+ F_2 - Y_- x F_3 - y^2 F_L], \quad (16)$$

where $Q^2 = xys$ and:

$$Y_+ = 1 + (1-y)^2, \quad Y_- = 1 - (1-y)^2 = 2y - y^2. \quad (17)$$

For W^- exchange on the proton ($e^-p \rightarrow \nu_e X$), the leading-order structure functions are:

$$F_2^{W^-}(x) = 2x [u(x) + c(x) + \bar{d}(x) + \bar{s}(x)], \quad (18)$$

$$xF_3^{W^-}(x) = 2x [u(x) + c(x) - \bar{d}(x) - \bar{s}(x)]. \quad (19)$$

Thus xF_3 is sensitive to the difference between quark and antiquark distributions, dominated by valence quarks at moderate x . These are the same structure functions probed by $\bar{\nu}_\mu p \rightarrow \mu^+ X$ (both involve W^- exchange), but the EIC measurement is on a *free proton* with known beam energy.

The key observation is that F_2 and xF_3 multiply different functions of y : at $y \rightarrow 0$, $Y_+ \rightarrow 2$ but $Y_- \rightarrow 0$, so only F_2 contributes; at $y \rightarrow 1$, both contribute equally. By fitting the y -distribution at fixed x , one extracts both $F_2(x)$ and $xF_3(x)$ simultaneously. We set $F_L = 0$ (Callan–Gross relation), valid at leading order; NLO corrections give $F_L \sim \mathcal{O}(\alpha_s/(4\pi)) \times F_2$, suppressed by the y^2 prefactor.

TABLE I. EIC parameters used in this analysis. All values from the EIC Yellow Report [27] unless otherwise noted.

Parameter	Value	Note
E_e	18 GeV	Maximum
E_p	275 GeV	Maximum
\sqrt{s}	140.7 GeV	
\mathcal{L}	$10^{34} \text{ cm}^{-2}\text{s}^{-1}$	Design
$\int \mathcal{L} dt$	500 fb^{-1}	5 years
Electron pol. P_e	80%	Longitudinal
Proton pol. P_p	70%	Longitudinal
Polarimetry unc.	1% (relative)	

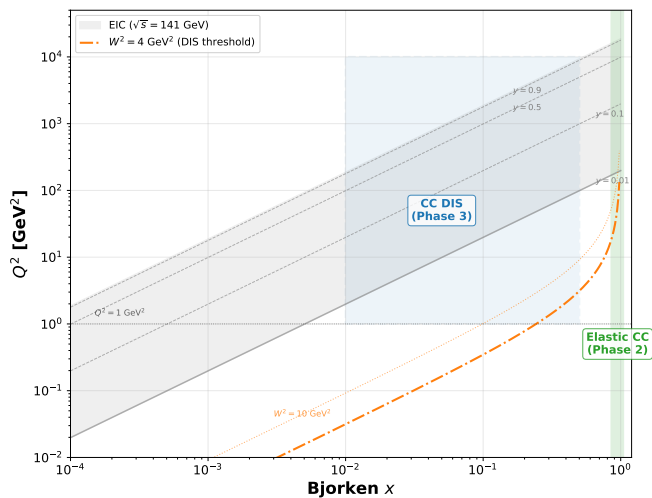


FIG. 2. Kinematic coverage of the EIC at $\sqrt{s} = 141$ GeV in the (x, Q^2) plane. Gray shading: accessible phase space for $0.01 < y < 0.95$. Green band: elastic CC region ($x \approx 1$). Blue dashed rectangle: CC DIS region used for xF_3 extraction. Orange dot-dashed line: $W^2 = 4 \text{ GeV}^2$ (DIS threshold). Diagonal gray lines: constant y .

III. EIC EXPERIMENTAL SETUP

A. Machine parameters

We assume the EIC at its maximum energy: $E_e = 18$ GeV colliding with $E_p = 275$ GeV, giving $\sqrt{s} = \sqrt{4E_e E_p} = 140.7$ GeV and $s = 19,800 \text{ GeV}^2$. The equivalent fixed-target energy is $E_e^* = s/(2M_p) \approx 10,554$ GeV. The parameters relevant to this analysis are summarized in Table I.

The kinematic coverage is shown in Fig. 2. The elastic CC channel corresponds to $x = 1$, $Q^2 \sim 0.01\text{--}3 \text{ GeV}^2$ (Phase 2), while CC DIS at $Q^2 > 1 \text{ GeV}^2$, $0.01 < x < 0.5$ provides the y -leverage for structure function extraction (Phase 3).

B. Signal topology and backgrounds

The elastic CC event $e^- p \rightarrow \nu_e n$ produces a forward neutron (detected in the Zero Degree Calorimeter, ZDC) and a neutrino (missing energy), with no scattered electron in the central detector. The signature is a leading neutron with $x_L = E_n/E_p > 0.88$ and no other activity, as studied by Klest [28].

The dominant background is *leading neutron photoproduction*: $\gamma^* p \rightarrow n\pi^+ X$, with a cross section $\sigma_{\text{bg}} \sim 0.3 \mu\text{b}$ [28], roughly 3×10^4 times larger than the CC elastic signal. Background rejection comes from: (i) a forward charged-particle veto (three silicon layers at 99.8% efficiency each) [28]; (ii) the $x_L > 0.88$ cut; and (iii) helicity filtering (Sec. V). After the veto and kinematic cuts, we estimate a combined background suppression factor of $\sim 10^{-4}$, yielding a residual background cross section $\sigma_{\text{bg}}^{\text{after}} \approx 30,000 \text{ fb}$ ($= 0.3 \mu\text{b} \times 10^{-4}$, using $1 \mu\text{b} = 10^9 \text{ fb}$).

IV. SENSITIVITY PROJECTION METHODOLOGY

All sensitivity projections in this paper use the Fisher information matrix formalism [33]. This section describes the method, inputs, and assumptions in detail.

A. Fisher information matrix

For a counting experiment with Poisson-distributed event counts N_k in bins k that depend on parameters θ_i , the Fisher information matrix is:

$$\mathcal{F}_{ij} = \sum_k \frac{1}{N_k(\boldsymbol{\theta})} \frac{\partial N_k}{\partial \theta_i} \frac{\partial N_k}{\partial \theta_j}. \quad (20)$$

The covariance matrix of the maximum-likelihood estimator is bounded from below by $C \geq \mathcal{F}^{-1}$ (the Cramér–Rao inequality), so $\delta\theta_i \geq \sqrt{(\mathcal{F}^{-1})_{ii}}$. Our projections report this lower bound. The Fisher approach assumes the Gaussian limit of Poisson statistics (valid for $N_k \gtrsim 10$) and linear parameter dependence near the minimum. With $\sim 1,440$ total events across 11 bins, most bins have $N_k \sim 50\text{--}300$, satisfying the Gaussian assumption. For a complete experimental analysis, a binned maximum-likelihood fit with Monte Carlo pseudo-experiments would be required to validate the Fisher projections; the purpose here is to establish the statistical feasibility of the measurement.

When an *asymmetry* A_k is also measured in each bin with Gaussian uncertainty δA_k , an additional Fisher contribution is:

$$\mathcal{F}_{ij}^{(A)} = \sum_k \frac{1}{(\delta A_k)^2} \frac{\partial A_k}{\partial \theta_i} \frac{\partial A_k}{\partial \theta_j}. \quad (21)$$

The total Fisher matrix is $\mathcal{F} = \mathcal{F}^{(\sigma)} + \mathcal{F}^{(A)}$.

TABLE II. Fixed physics inputs used in the sensitivity projections.

Quantity	Value	Source
G_F	$1.1664 \times 10^{-5} \text{ GeV}^{-2}$	PDG [21]
$ V_{ud} $	0.97373	PDG [21]
M (nucleon avg)	0.939 GeV	PDG [21]
M_W	80.377 GeV	PDG [21]
g_A (fiducial)	1.2723	PDG [21]
M_A (fiducial)	1.026 GeV	Ref. [22]
M_V^2	0.71 GeV ²	Electron scattering
μ_p	2.793	PDG [21]
μ_n	-1.913	PDG [21]
s	19,800 GeV ²	EIC 18 \times 275
\mathcal{L}_{int}	500 fb ⁻¹	5 years
P_p	0.70	EIC YR [27]

B. Inputs and assumptions

The following assumptions apply throughout:

a. Event counting. The expected number of elastic CC events in Q^2 bin k is:

$$N_k = \frac{1}{2} \mathcal{L}_{\text{int}} \left. \frac{d\sigma}{dQ^2} \right|_{Q_k^2} \Delta Q_k^2, \quad (22)$$

where the factor 1/2 accounts for the fact that only left-handed electrons produce CC interactions (Sec. V), and we assume 50% of the delivered luminosity is in each helicity state. The cross section $d\sigma/dQ^2$ is evaluated at the bin center using the Llewellyn Smith formula (11) with fixed inputs from Table II.

b. Asymmetry uncertainty. The statistical uncertainty on the target-spin asymmetry in each Q^2 bin is:

$$\delta A_{UL,k} = \frac{1}{P_p \sqrt{N_k}}, \quad (23)$$

where $P_p = 0.70$ is the proton beam polarization and N_k is the number of CC events in the bin. This follows from $\text{Var}(A_{\text{meas}}) \approx 1/N$ for the raw counting asymmetry, with the physical asymmetry diluted by the polarization: $A_{\text{meas}} = P_p \cdot A_{\text{true}}$.

c. Numerical derivatives. Partial derivatives $\partial N_k/\partial\theta_i$ and $\partial A_k/\partial\theta_i$ are computed by central finite differences with a 1% step size in each parameter (e.g., $\Delta g_A = 0.01 \times g_A$). We have verified that the results are insensitive to the step size over the range 0.1–5%.

d. Binning. For elastic CC: 11 logarithmically spaced Q^2 bins from 0.01 to 3.0 GeV². For CC DIS: 19 uniform y bins from 0.05 to 0.95, with x -bin width $\Delta x = 0.05$.

C. Realistic detector model

In addition to the ideal (Cramér–Rao) projections, we present a first-order realistic estimate that incorporates

TABLE III. Detector model parameters for the realistic projection.

Parameter	Value	Source
<i>ZDC acceptance for elastic neutrons</i>		
Core acceptance ($\theta_n < 3.5$ mrad)	85%	YR [27]
Edge falloff	3.5–5.5 mrad	YR [27]
<i>Efficiency factors</i>		
ZDC trigger	95%	
$x_L > 0.88$ cut (signal)	99%	
Analysis quality cuts	90%	
<i>Kinematic resolution</i>		
$\sigma(Q^2)/Q^2$	5%	Ref. [28]
<i>Systematic uncertainties</i>		
Luminosity	2% (relative)	YR [27]
Polarimetry (P_p)	1% (relative)	YR [27]
ZDC energy scale	1% (relative)	
LH/RH bg subtraction	1% of N_{bg}	

detector effects. The model parameters (Table III) are based on the EIC Yellow Report [27] and Klest [28].

a. ZDC acceptance. The elastic neutron angle in the lab frame is $\theta_n \approx \sqrt{Q^2}/E_p$. For $Q^2 = 1 \text{ GeV}^2$, $\theta_n \approx 3.6$ mrad; for $Q^2 = 2 \text{ GeV}^2$, $\theta_n \approx 5.1$ mrad. The ZDC has full efficiency ($\varepsilon_{\text{ZDC}} \approx 85\%$, accounting for shower containment and dead material) for $\theta_n < 3.5$ mrad, linearly falling to zero at $\theta_n = 5.5$ mrad. Combined with trigger (95%), x_L cut (99%), and analysis (90%) efficiencies, the total detection efficiency is $\varepsilon \approx 72\%$ for $Q^2 \lesssim 0.9 \text{ GeV}^2$, dropping to zero for $Q^2 \gtrsim 2.3 \text{ GeV}^2$. The effective number of detected CC events is $\sim 1,440$ (compared to $\sim 2,200$ in the ideal case).

b. Q^2 smearing. The Q^2 resolution of $\sim 5\%$ [28] causes bin migration in the Q^2 -binned cross section. We model this with a Gaussian response matrix R_{kj} where R_{kj} is the probability that a true- Q^2 event in bin j is reconstructed in bin k . The smeared expected events are $N_k^{\text{reco}} = \sum_j R_{kj} N_j^{\text{true}}$.

c. Background in the Fisher matrix. After helicity subtraction (26), the expected CC signal in each bin is unbiased, but the *variance* is $\sigma_k^2 = S_k + 2B_k$ where S_k is the signal and B_k is the background per helicity. The Fisher information is therefore $\mathcal{F}_{ij}^{(\sigma)} = \sum_k (\partial S_k/\partial\theta_i)(\partial S_k/\partial\theta_j)/(S_k + 2B_k)$, which is degraded by the factor $S_k/(S_k + 2B_k) \approx 0.07$ – 0.21 relative to the ideal case (varies by Q^2 bin). Similarly, the asymmetry uncertainty including background dilution is $\delta A_k = \sqrt{(S_k + 2B_k)/(P_p S_k)}$, degraded by $\sqrt{1 + 2B_k/S_k}$ compared to the signal-only case.

d. Systematic uncertainties. For each source listed in Table III, we propagate the assumed uncertainty to M_A by computing the bias from a 1σ shift:

- *Luminosity (2%)*: scales the overall event count, affecting the cross section normalization. Since M_A is extracted from the Q^2 shape, the impact is small: $\delta M_A = 0.004 \text{ GeV}$.

- *ZDC energy scale* (1%): shifts $Q_{\text{reco}}^2 \rightarrow Q_{\text{true}}^2(1 + \delta_E)$, distorting the Q^2 shape. This is a significant systematic: $\delta M_A = 0.012 \text{ GeV}$.
- *Polarimetry* (1%): affects the extracted A_{UL} asymmetry. Since the cross section shape dominates over A_{UL} in the realistic projection (due to background dilution), the impact is small: $\delta M_A = 0.001 \text{ GeV}$.
- *Background subtraction* (1% LH/RH asymmetry): imperfect helicity subtraction from LH/RH luminosity imbalance injects a residual with the exponential background Q^2 shape. This is the largest systematic: $\delta M_A = 0.015 \text{ GeV}$.

The total systematic $\delta M_A^{\text{syst}} = 0.019 \text{ GeV}$ (added in quadrature) is subdominant to the statistical+detector uncertainty. The systematic budget is summarized in Table VI in Sec. VIII B.

e. What is not included. The following effects are still omitted in both projections:

1. *QCD corrections.* The elastic cross section is computed at tree level. The DIS cross section uses leading-order structure functions with $F_L = 0$ (Callan–Gross) and toy PDFs at a fixed scale (Appendix B). NLO QCD and DGLAP evolution are omitted.
2. *Radiative corrections.* QED corrections to the CC vertex are $\mathcal{O}(\alpha/\pi) \sim 0.2\%$ and negligible.
3. *Full detector simulation.* The response matrix and efficiency models are parameterized, not from Geant4.
4. *Unfolding.* We assume perfect bin-center corrections; a real analysis would require iterative unfolding.

V. PHASE 1: HELICITY FILTERING

A. Principle

The W boson couples exclusively to left-handed fermions. CC interactions can therefore only occur with LH electrons, while electromagnetic processes occur with both helicities. The EIC stores alternating bunches of longitudinally polarized electrons. For an electron beam polarization $P_e = 0.80$:

- “LH bunches” contain $(1 + P_e)/2 = 90\%$ LH and 10% RH electrons;
- “RH bunches” contain $(1 - P_e)/2 = 10\%$ LH and 90% RH electrons.

Recording data separately:

$$N_{\text{LH}} = \frac{1+P_e}{2} N_{\text{CC}} + N_{\text{EM}}, \quad (24)$$

$$N_{\text{RH}} = \frac{1-P_e}{2} N_{\text{CC}} + N_{\text{EM}}, \quad (25)$$

the CC signal is extracted by polarization-corrected subtraction:

$$N_{\text{CC}} = \frac{N_{\text{LH}} - N_{\text{RH}}}{P_e}, \quad (26)$$

with statistical uncertainty $\delta N_{\text{CC}} = \sqrt{N_{\text{LH}} + N_{\text{RH}}}/P_e$. The factor $1/P_e$ arises because the subtraction $N_{\text{LH}} - N_{\text{RH}}$ yields $(P_e) \cdot N_{\text{CC}}$, not N_{CC} directly. For $P_e = 0.80$, this correction factor is $1/0.80 = 1.25$, meaning: (i) the raw subtraction underestimates N_{CC} by 20% if uncorrected, and (ii) the statistical uncertainty is amplified by the same factor, $\delta N_{\text{CC}} \propto 1/P_e$. Higher polarization reduces this amplification and improves sensitivity.

B. Background model and pseudo-data generation

To illustrate the helicity filtering, we generate pseudo-data with the following model:

- *Signal:* CC elastic events from the Llewellyn Smith formula (11) with $M_A = 1.026 \text{ GeV}$, counted per Eq. (22) with $\mathcal{L}_{\text{LH}} = 250 \text{ fb}^{-1}$.
- *Background:* The residual photoproduction background (after forward veto and x_L cut) with total cross section $\sigma_{\text{bg}}^{\text{after}} \approx 30,000 \text{ fb}$ ($= 0.3 \mu\text{b} \times 10^{-4}$, using $1 \mu\text{b} = 10^9 \text{ fb}$). The Q^2 shape is modeled as an exponential:

$$\frac{d\sigma_{\text{bg}}}{dQ^2} = \frac{\sigma_{\text{bg}}^{\text{after}}}{\Lambda^2} e^{-Q^2/\Lambda^2}, \quad \Lambda^2 = 0.3 \text{ GeV}^2, \quad (27)$$

reflecting the quasi-real photon origin ($Q^2 \rightarrow 0$). This shape is an ansatz; the helicity subtraction removes it regardless of the true shape.

- *Poisson sampling:* The expected event counts $\langle N_k \rangle$ in each Q^2 bin are computed from the cross section \times luminosity. The *observed* counts are then drawn from Poisson distributions: $N_k \sim \text{Poisson}(\langle N_k \rangle)$. This standard Monte Carlo procedure produces statistical fluctuations around the true expectation, representing what an actual experiment would observe. In Fig. 3, the deviations of the black data points from the green histogram reflect these Poisson fluctuations.

C. Results

Figure 3 shows the result. With 500 fb^{-1} total luminosity split equally between helicity states (250 fb^{-1} per helicity), $\sim 2,200$ CC events are produced (all from LH electrons) alongside $\sim 7.5 \times 10^6$ background events per helicity (signal-to-background ratio $S/B \approx 3 \times 10^{-4}$). The helicity subtraction recovers the CC signal within statistical uncertainties. The $1/\sqrt{N_{\text{LH}} + N_{\text{RH}}}$ errors are

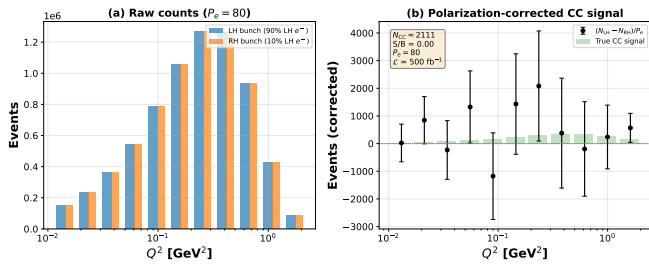


FIG. 3. Helicity filtering for CC elastic signal extraction (500 fb^{-1} total, 250 fb^{-1} per helicity, $P_e = 0.80$). *Left*: Raw event counts by electron helicity. With 80% polarization, LH bunches contain 90% LH electrons and RH bunches contain 10% LH electrons, so both produce CC events. *Right*: Polarization-corrected CC signal $(N_{\text{LH}} - N_{\text{RH}})/P_e$ (black points with error bars) compared to the true CC signal (green bars). The error bars include the $1/P_e$ amplification factor per Eq. (26). Statistical fluctuations arise from Poisson sampling (Sec. VB). Background: exponential in Q^2 with $30,000 \text{ fb}$ total cross section after veto cuts ($S/B \approx 3 \times 10^{-4}$).

driven by the total event count in each bin, including both signal and background.

We emphasize that the background model only affects Fig. 3; the Fisher projections in Sec. VI use signal-only event counts and assume perfect background subtraction.

VI. PHASE 2: AXIAL FORM FACTOR MEASUREMENT

A. A_{UL} sensitivity to M_A

Figure 4 shows $|A_{UL}(Q^2)|$ for four values of M_A : 0.90, 1.03, 1.10, and 1.35 GeV. At low Q^2 , all curves converge to $|A_{UL}| \approx 1$. In the sensitivity window $Q^2 \sim 0.1$ – 1 GeV^2 , the curves separate: larger M_A produces a flatter $F_A(Q^2)$, keeping $|A_{UL}|$ high to larger Q^2 .

The error bars show the projected EIC statistical precision from Eq. (23), evaluated in 9 logarithmically spaced Q^2 bins from 0.03 to 2.5 GeV^2 . Black circles show the ideal case ($\sim 2,200$ events, no background), with per-bin precision $\delta A_{UL} \sim 0.06$ – 0.15 . With the corrected $S/B \approx 3 \times 10^{-4}$, the realistic asymmetry uncertainty is $\delta A_{UL} \sim 1$ – 10 —far exceeding $|A_{UL}| \lesssim 1$ and providing essentially no constraint. The asymmetry measurement would only become useful with background suppression approaching 10^{-7} .

B. Fisher matrix projection

We project the precision on $\theta = (g_A, M_A)$ using two information sources, as described in Sec. IV A.

a. Cross section shape ($\mathcal{F}^{(\sigma)}$). The expected events $N_k(g_A, M_A)$ in 11 Q^2 bins are computed from Eq. (22). The sensitivity enters through the Q^2 dependence: in-

TABLE IV. Projected 1σ uncertainties on (g_A, M_A) from the elastic CC channel with 500 fb^{-1} and $P_p = 0.70$. The ideal projection uses signal-only Poisson statistics (Cramér–Rao floor). The realistic projection includes ZDC acceptance, Q^2 smearing, background noise from helicity subtraction, and systematic uncertainties.

	δg_A	δM_A [GeV]	ρ
<i>Ideal (Cramér–Rao floor, $\sim 2,200$ events)</i>			
$d\sigma/dQ^2$ only	0.046 (3.6%)	0.033 (3.2%)	−0.80
A_{UL} only	0.56 (44%)	0.27 (26%)	−0.77
Combined	0.045 (3.6%)	0.032 (3.2%)	−0.79
<i>Realistic ($\sim 1,400$ signal, $S/B \approx 3 \times 10^{-4}$)</i>			
Stat.+detector	5.9 (470%)	3.9 (380%)	−0.84
Systematic	0.019	0.019	—
Total	5.9 (470%)	3.9 (380%)	−0.84
(Measurement unfeasible with 10^{-4} background suppression)			

creasing g_A raises F_A at all Q^2 (changing the normalization), while increasing M_A flattens the Q^2 slope (changing the shape). Numerical derivatives $\partial N_k/\partial g_A$ and $\partial N_k/\partial M_A$ are evaluated by re-computing the full Llewellyn Smith cross section at shifted parameter values.

b. Target-spin asymmetry ($\mathcal{F}^{(A)}$). A_{UL} is computed from the full Dirac trace at each shifted (g_A, M_A) point. The asymmetry is a *ratio* of spin-dependent cross sections, so it is insensitive to the overall normalization but directly constrains the relative V–A interference.

c. Combined result. The total Fisher matrix $\mathcal{F} = \mathcal{F}^{(\sigma)} + \mathcal{F}^{(A)}$ is inverted to give the projected uncertainties (Table IV).

The ideal result $\delta M_A = 0.032 \text{ GeV}$ (3.2%) is dominated by the Q^2 -binned cross section rather than the asymmetry. With only $\sim 2,200$ events, the per-bin asymmetry measurement has limited statistical power, while the cross section shape provides a direct measurement of F_A^2 in each bin. Quantitatively, decomposing the Fisher information: the cross-section shape contributes $\sim 98\%$ of the total information on M_A , while A_{UL} contributes only $\sim 2\%$. The asymmetry measurement is therefore a complementary probe rather than the primary sensitivity driver. The value of A_{UL} lies in its different systematic dependencies (it is a ratio, so luminosity uncertainties cancel), providing a cross-check rather than the dominant constraint.

The *realistic* projection degrades the sensitivity catastrophically, from $\delta M_A = 0.032 \text{ GeV}$ (statistical floor) to $\delta M_A \gg 1 \text{ GeV}$. The dominant effect is the background noise from helicity subtraction: with $S/B \approx 3 \times 10^{-4}$, the effective variance per bin is $S + 2B \approx 6,700 S$, degrading the Fisher information by nearly four orders of magnitude. The ZDC acceptance loss (reducing events from $\sim 2,200$ to $\sim 1,440$) and Q^2 smearing have modest additional impact. Systematic uncertainties total $\delta M_A^{\text{sys}} = 0.019 \text{ GeV}$, dominated by the ZDC energy scale (0.012 GeV) and residual background sub-

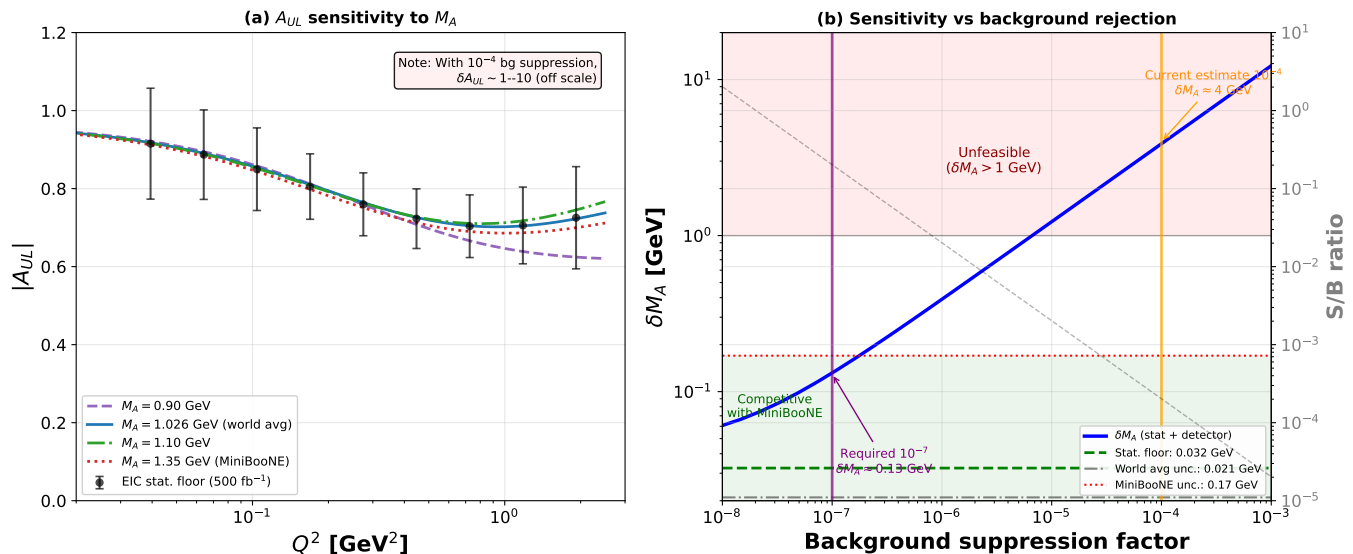


FIG. 4. (a) Target-spin asymmetry $|A_{UL}|$ vs Q^2 for different M_A values. The curves separate in the sensitivity window $0.1 < Q^2 < 1$ GeV². Black circles: ideal statistical floor. With 10^{-4} background suppression, the asymmetry uncertainties are $\delta A_{UL} \sim 1-10$ (off scale), providing no constraint. (b) Projected δM_A vs background suppression factor over the full range. The measurement is severely background-limited: the current baseline (10^{-4}) yields $\delta M_A \approx 4$ GeV (unfeasible). Achieving $\delta M_A \lesssim 0.17$ GeV (MiniBooNE precision) requires 10^{-7} suppression. The green and red shaded regions indicate competitive and unfeasible regimes, respectively.

traction (0.015 GeV), and are subdominant to the statistical+detector contribution.

Improving the background suppression by orders of magnitude is essential:

- 10^{-5} : $\delta M_A \approx 1.3$ GeV (still unfeasible)
- 10^{-6} : $\delta M_A \approx 0.4$ GeV (marginal)
- 10^{-7} : $\delta M_A \approx 0.14$ GeV (competitive)

Achieving 10^{-7} suppression (three orders of magnitude beyond baseline) represents an extraordinary experimental challenge.

Regarding the physics reach: the MiniBooNE anomaly corresponds to a shift of $\Delta M_A = 1.35 - 1.03 = 0.32$ GeV. With the statistical floor $\delta M_A = 0.032$ GeV, an EIC measurement (if backgrounds can be sufficiently suppressed) centered on the world average would disfavor the MiniBooNE value at $0.32/0.032 \approx 10\sigma$. With the more realistic 10^{-7} suppression ($\delta M_A = 0.14$ GeV), this becomes $0.32/0.14 \approx 2.3\sigma$. The key value of the EIC measurement is not merely the precision, but that it is performed on a *free proton*, eliminating the nuclear model uncertainties that complicate the interpretation of the MiniBooNE result.

Figure 5 shows the confidence ellipses for different background suppression scenarios. The ellipses exhibit a negative correlation between g_A and M_A : the cross section scales as $\sigma \propto g_A^2$ at low Q^2 , while the Q^2 shape depends on M_A through $(1 + Q^2/M_A^2)^{-4}$. A simultaneous increase in g_A and decrease in M_A (or vice versa)

can produce similar cross sections over the measured Q^2 range, hence the tilted ellipse.

The coupling $g_A = F_A(0) = 1.2723 \pm 0.0023$ is independently determined from neutron beta decay [21] with 0.2% precision—far better than any scattering experiment can achieve. Previous CCQE measurements therefore fix g_A to this external value and fit only M_A from the Q^2 shape. The projected δM_A values in Table IV follow this approach: they correspond to projecting the 2D ellipse onto the M_A axis using the external g_A constraint. In Figure 5, the purple band shows the g_A constraint from neutron decay; the intersection with each ellipse determines the effective M_A uncertainty.

We emphasize that the EIC is not intended to measure g_A more precisely than neutron beta decay. Rather, the analysis uses g_A as an external input (a Bayesian prior) to extract M_A —the same approach used by all neutrino experiments. The value of the EIC measurement is that it provides a consistency check: if the beta-decay g_A , when used in CC scattering on a free proton, yields an M_A consistent with the deuterium world average, this confirms the Standard Model V–A structure across different processes. Conversely, a significant discrepancy would signal new physics or unaccounted systematic effects. We acknowledge that this consistency check is not fully independent: since g_A is used as an input to extract M_A , the two parameters cannot be determined simultaneously with competitive precision. The measurement tests whether the (g_A, M_A) values from beta decay and CC scattering are mutually consistent, rather than providing independent determinations of both.

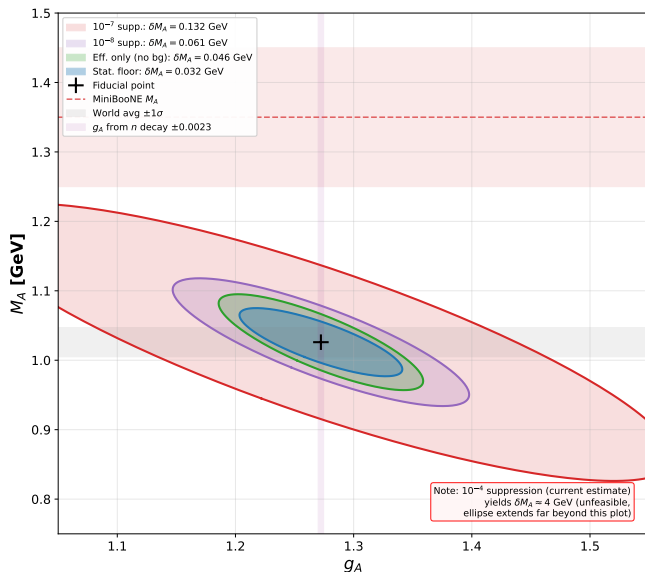


FIG. 5. Projected 1σ confidence contours in the (g_A, M_A) plane for achievable suppression scenarios. Blue: statistical floor (Cramér–Rao bound, $\delta M_A = 0.032$ GeV). Green: efficiency only, no background ($\delta M_A = 0.045$ GeV). Purple: aggressive R&D scenario with 10^{-8} suppression. Red: minimum viable 10^{-7} suppression ($\delta M_A \approx 0.13$ GeV). The current baseline (10^{-4}) yields $\delta M_A \approx 4$ GeV—the ellipse would extend far beyond the plot and is not shown. The purple vertical band shows the external g_A constraint from neutron beta decay. Contours use $\Delta\chi^2 = 2.30$ for two parameters.

Regarding the background rejection requirement: the baseline 10^{-4} suppression yields $S/B \approx 3 \times 10^{-4}$, making the measurement unfeasible. To achieve $S/B \approx 0.1$ and $\delta M_A \approx 0.14$ GeV, a background suppression of $\sim 10^{-7}$ would be required—three orders of magnitude beyond current projections. We identify aggressive background reduction as the critical challenge for this measurement.

VII. PHASE 3: STRUCTURE FUNCTION EXTRACTION

A. The y -distribution method

The principle underlying $x F_3$ extraction is similar to Rosenbluth separation in elastic electron scattering: the cross section is a linear combination of two unknown quantities (G_E and G_M , or here F_2 and $x F_3$), each multiplied by a known kinematic function. By measuring at multiple kinematic points where the coefficients differ, one can disentangle the two contributions.

In CC DIS, the role of the scattering angle is played by the inelasticity y . At fixed Bjorken x , the cross section (16) is *linear* in F_2 and $x F_3$:

$$N_i = \alpha_i [Y_+(y_i) F_2 - Y_-(y_i) x F_3], \quad (28)$$

where $\alpha_i = \frac{1}{2} \mathcal{L} P(y_i) \Delta x \Delta y_i$ contains the known

prefactors including the W propagator $P(y) = (G_F^2 s / 4\pi) (M_W^2 / (Q^2 + M_W^2))^2$. The functions $Y_+ = 1 + (1-y)^2$ and $Y_- = 2y - y^2$ have different y -shapes: Y_+ peaks at both $y = 0$ and $y = 1$, while Y_- vanishes at $y = 0$ and peaks at $y = 1$. Fitting the observed y -distribution across many bins separates the F_2 and $x F_3$ contributions, analogous to how varying the electron scattering angle separates G_E and G_M in elastic scattering.

The Fisher matrix for $\theta = (F_2, x F_3)$ at fixed x has analytical derivatives:

$$\frac{\partial N_i}{\partial F_2} = \alpha_i Y_{+,i}, \quad \frac{\partial N_i}{\partial (x F_3)} = -\alpha_i Y_{-,i}, \quad (29)$$

giving the 2×2 Fisher matrix:

$$\mathcal{F} = \sum_i \frac{1}{N_i} \begin{pmatrix} (\alpha_i Y_{+,i})^2 & -\alpha_i^2 Y_{+,i} Y_{-,i} \\ -\alpha_i^2 Y_{+,i} Y_{-,i} & (\alpha_i Y_{-,i})^2 \end{pmatrix}. \quad (30)$$

The structure functions F_2 and $x F_3$ are computed from the toy PDF parameterization (Appendix B). The absolute values are approximate; the relevant feature for the sensitivity estimate is the $x F_3 / F_2$ ratio, which determines how strongly the Y_- term perturbs the y -distribution.

The CC DIS cross section is large: $\sigma_{\text{CC}}(Q^2 > 1 \text{ GeV}^2) \approx 105 \text{ pb}$, yielding $\sim 2.6 \times 10^7$ events with 500 fb^{-1} . Even in fine (x, y) bins, the per-bin statistics are $\mathcal{O}(10^4)$ – $\mathcal{O}(10^5)$.

B. Results

Figure 6 shows the y -distributions at $x = 0.1$ and $x = 0.3$, decomposed into $Y_+ F_2$ and $Y_- x F_3$ components. At $x = 0.1$, $x F_3 / F_2 = 0.58$ (significant sea); at $x = 0.3$, $x F_3 / F_2 = 0.92$ (valence-dominated).

The lower-right panel shows the projected extraction precision vs x . F_2 is constrained to $\sim 0.1\%$ over most of the x range. $x F_3$ is extracted to 0.2–0.4% for $x > 0.05$, but degrades to $\sim 7\%$ at $x = 0.01$ where $x F_3 / F_2 \rightarrow 0$. At small x the sea dominates, $x F_3 \approx 0$, and the $x F_3$ signal becomes a tiny perturbation on the dominant $Y_+ F_2$ term.

a. Theoretical limitations. The sub-percent statistical precision quoted above represents the Cramér–Rao floor, not the achievable experimental precision. In practice, the extraction is limited by: (i) QED radiative corrections, which distort the y -distribution at the few-percent level and must be unfolded using Monte Carlo; (ii) NLO QCD corrections to the structure functions and the Callan–Gross relation ($F_L \neq 0$); (iii) higher-twist effects at moderate Q^2 . A realistic estimate, accounting for these theoretical systematics, is $\delta(x F_3) / x F_3 \sim 2$ –5% (Table V). The statistical floor demonstrates that the EIC has ample event rates; the challenge is controlling the theoretical uncertainties.

TABLE V. Comparison of M_A and xF_3 measurements. EIC projections include both the ideal statistical floor and the realistic estimate with detector effects. NuTeV and CHORUS uncertainties include full systematic and nuclear corrections.

Experiment	Target	δM_A	Note
D ₂ bubble ch.	Free nucleon	± 0.021 GeV	World avg
MiniBooNE	Carbon	± 0.17 GeV	$M_A \approx 1.35$ GeV
MINERvA	Hydrogen	–	Limited stats
EIC (ideal)	Free p	± 0.032 GeV	Stat. floor
EIC (stat. floor)	Free p	± 0.032 GeV	Ideal
$\delta(xF_3)/xF_3$			
NuTeV [31]	Iron	5–10%	Full syst.
CHORUS [32]	Lead	$\sim 10\%$	Full syst.
EIC (ideal)	Free p	$< 1\%$	Stat. only
EIC (realistic)	Free p	2–5%	Est. syst.[†]

[†]Estimated including radiative corrections and detector resolution; requires full Monte Carlo study.

b. NC DIS background. The main experimental background for CC DIS is neutral-current (NC) DIS where the scattered electron is lost (undetected in a crack, down the beam pipe, or misidentified as a hadron). For $Q^2 > 1$ GeV², the electron scattering angle is $\theta_e \gtrsim 4^\circ$, well within the ePIC central detector acceptance, so electron detection efficiency exceeds 99%. With $\sigma_{\text{NC}}/\sigma_{\text{CC}} \sim 3\text{--}5$, the raw NC contamination is a few percent. This can be further suppressed by requiring large missing transverse momentum: CC events have $p_T^{\text{miss}} \sim 10\text{--}50$ GeV (the neutrino), while NC events with a lost electron have $p_T^{\text{miss}} \sim \sqrt{Q^2} \sim 1\text{--}5$ GeV. After a $p_T^{\text{miss}} > 10$ GeV cut, the residual NC contamination is $\lesssim 1\%$, yielding $S/B \gtrsim 100$. This contrasts sharply with the elastic channel, where $S/B \sim 10^{-4}$ before any kinematic cuts. The NC background dilutes the xF_3 signal (since NC has no parity-violating xF_3 from photon exchange), but the sub-percent contamination level is smaller than the theoretical systematics and can be corrected using measured electron veto efficiencies.

VIII. DISCUSSION

A. Comparison with neutrino experiments

Table V compares the projected EIC measurements with existing experiments.

The EIC measurements have two fundamental advantages: (1) a *free proton target*, eliminating the nuclear model uncertainties that affect all current precise xF_3 measurements; and (2) a *known beam*, eliminating the 5–10% neutrino flux uncertainties.

TABLE VI. Systematic uncertainty budget for δM_A in the realistic projection.

Source	Assumption	δM_A [GeV]
Background subtraction	1% LH/RH asymmetry	0.015
ZDC energy scale	1%	0.012
Luminosity	2%	0.004
Polarimetry (P_p)	1%	0.001
Total (quadrature)		0.019

B. Systematic uncertainties and their impact

Table VI summarizes the systematic uncertainty budget for the realistic M_A projection. The total systematic $\delta M_A^{\text{syst}} = 0.019$ GeV would be subdominant to the statistical floor of 0.032 GeV in the ideal case. However, with realistic background levels ($S/B \approx 10^{-4}$), systematic uncertainties are entirely negligible. The methodology for propagating each source is described in Sec. IV C.

a. Hierarchy of uncertainties. The dominant uncertainty source is statistical noise from the helicity subtraction ($S + 2B$ variance), followed by ZDC acceptance loss. Systematic uncertainties are currently subdominant. Even with 10^{-7} background suppression (yielding $\delta M_A \approx 0.14$ GeV), the ZDC energy scale and background subtraction would each contribute $\sim 0.01\text{--}0.02$ GeV, remaining subdominant.

b. Paths to improvement. The background subtraction systematic could be reduced by improved LH/RH luminosity monitoring or by using the RH data to directly constrain the background Q^2 shape (currently we assume the shape is known). The ZDC energy scale could be calibrated using exclusive $\pi^0 \rightarrow \gamma\gamma$ decays or the $\eta \rightarrow \gamma\gamma$ peak. Radiative corrections can be computed with existing tools (RADCOR) and unfolded.

c. Form factor model dependence. The dipole *ansatz* for $F_A(Q^2)$ is conventional but not fundamental. Model-independent extractions using the z-expansion [22] parameterization could be performed with the same data, at the cost of additional fit parameters. The vector form factor uncertainties (1–2% [30]) contribute a small additional systematic not included in Table VI.

C. Nuclear targets

The EIC will collide electrons with nuclear beams (d, He, C, Ca, Pb), enabling a direct measurement of the A -dependence of CC scattering. This could explain the MiniBooNE anomaly as a nuclear effect.

To illustrate one component of nuclear effects, we apply a local Fermi gas model [34] with Pauli blocking. In a nucleus, the final-state neutron must have momentum above the Fermi surface ($k_F \approx 225$ MeV for $A \geq 12$). This blocks low- Q^2 events where the three-momentum

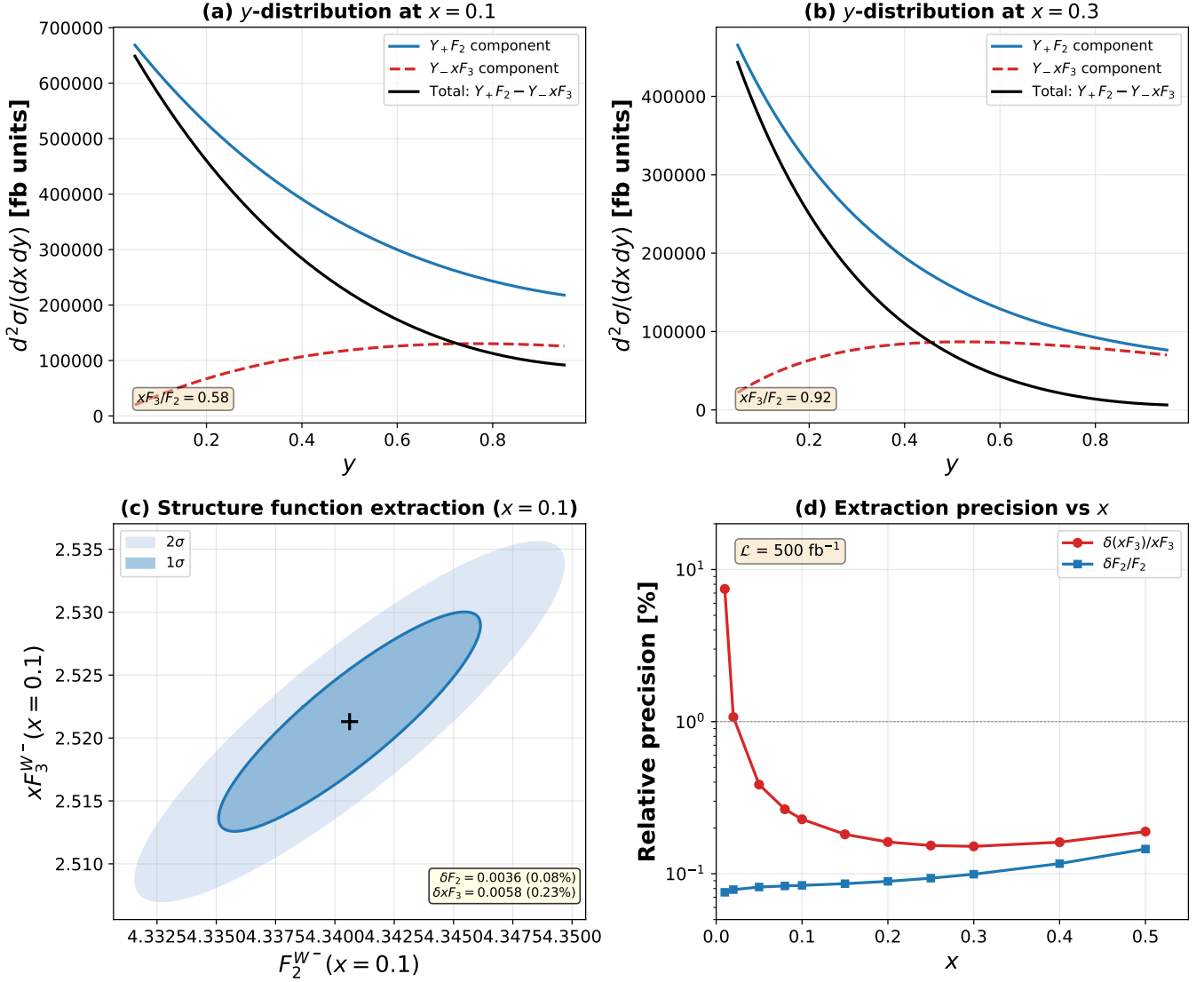


FIG. 6. CC DIS y -leverage for $x F_3$ extraction (all projections: 500 fb^{-1} , statistical only). *Upper*: y -distributions at $x = 0.1$ (left) and $x = 0.3$ (right), decomposed into $Y_+ F_2$ (blue) and $Y_- x F_3$ (red dashed) components. Structure functions from toy PDFs (Appendix B). *Lower left*: Fisher-projected confidence ellipse for $(F_2, x F_3)$ at $x = 0.1$ in 19 y -bins. *Lower right*: Relative extraction precision vs x , showing sub-percent $x F_3$ extraction for $x > 0.05$.

transfer $|\vec{q}| < 2k_F$, preferentially removing events where F_A is largest.

Figure 7 shows the result. The per-nucleon cross section decreases with A due to Pauli blocking (left panel). When the nuclear-modified Q^2 distribution is fit with the free-nucleon formula, the extracted M_A^{eff} exceeds the true value (right panel): Pauli blocking removes the low- Q^2 events that anchor F_A , mimicking a harder (more slowly falling) form factor. For carbon ($A = 12$), Pauli blocking alone shifts M_A^{eff} upward by ~ 0.1 – 0.2 GeV.

We emphasize that this is a simplified illustration. The modern consensus [25, 26] attributes the MiniBooNE anomaly primarily to *two-particle-two-hole* ($2p2h$) excitations and meson exchange currents, which are not included in the simple Fermi gas model. These multi-

nucleon correlations produce additional cross section enhancement at moderate Q^2 that mimics CCQE events and further inflates M_A^{eff} . A full treatment requires sophisticated many-body calculations beyond the scope of this paper. The key point is that measurements on nuclear targets cannot straightforwardly extract the free-nucleon M_A . In contrast, the EIC provides a clean probe on a free proton.

D. Caveats and future improvements

This sensitivity study relies on several approximations that should be addressed in future work:

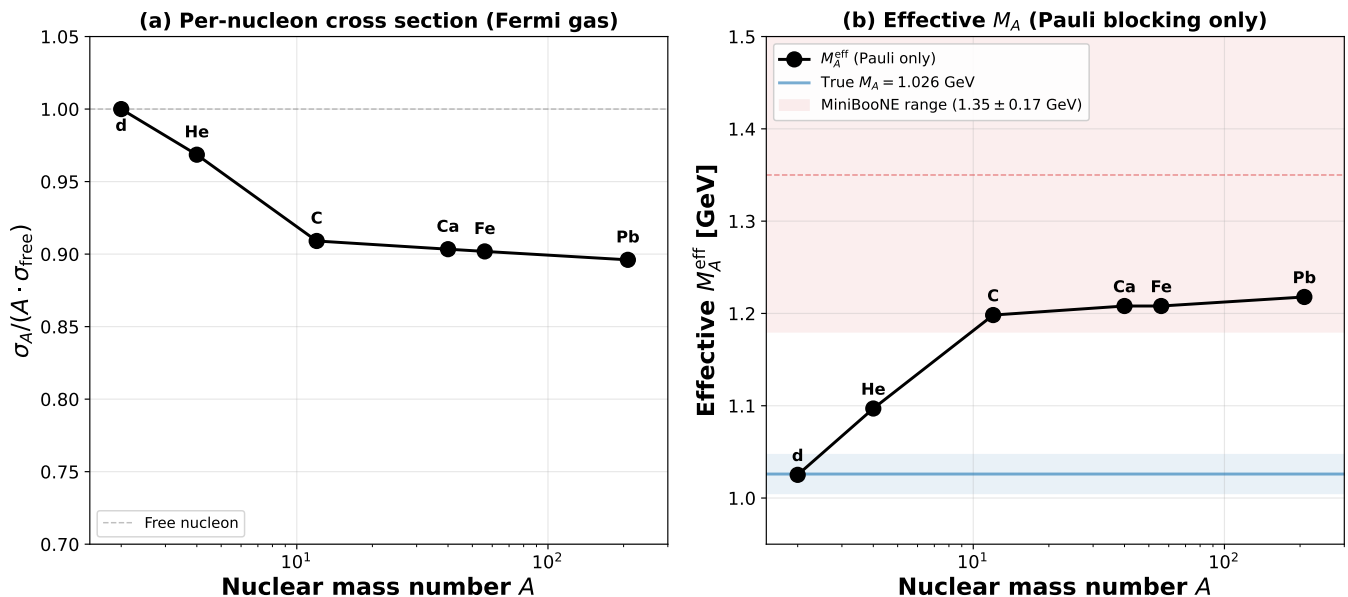


FIG. 7. Illustrative nuclear target scaling using a simplified local Fermi gas model [34] with Pauli blocking only. *Left:* Per-nucleon cross section ratio $\sigma_A/(A \cdot \sigma_{\text{free}})$ vs A , showing Pauli blocking suppression. *Right:* Effective M_A^{eff} extracted by fitting the nuclear-modified Q^2 shape with the free-nucleon formula. The blue band is the true $M_A = 1.026$ GeV; the red band is the MiniBooNE range (1.35 \pm 0.17 GeV). Note: This simplified model shows only Pauli blocking; the full MiniBooNE anomaly is primarily attributed to 2p2h/MEC effects (Sec. VIII C), which produce larger shifts than shown here.

a. Background model. The photoproduction background is modeled as an exponential $dN/dQ^2 \propto \exp(-Q^2/\Lambda^2)$ with $\Lambda^2 = 0.3 \text{ GeV}^2$, based on pion-exchange phenomenology. The 10^{-4} suppression factor is from Ref. [28]; the actual achievable suppression depends critically on the forward veto design and hadron rejection algorithms. The veto strategy relies on detecting the π^+ from $\gamma^*p \rightarrow n\pi^+X$ in the forward tracker; at very low Q^2 (quasi-real photoproduction), the scattered electron remains in the beam pipe and cannot be used for rejection. Additionally, *beam-gas backgrounds*—electrons scattering off residual gas in the vacuum pipe—can produce fake CC signatures (neutrons and missing energy) and are not included in this analysis. A full GEANT4 simulation with realistic detector response and vacuum conditions is needed to validate these estimates.

b. ZDC acceptance. We use a simplified ZDC model with a plateau efficiency of 85% for $\theta_n < 3.5$ mrad and linear falloff to zero at 5.5 mrad. The actual acceptance depends on the beam optics, magnet apertures, and hadronic shower containment. The beam-pipe hole at $\theta = 0$ may affect the lowest- Q^2 bin.

c. Dipole form factor assumption. The analysis assumes $F_A(Q^2) = g_A/(1 + Q^2/M_A^2)^2$. The z-expansion formalism [22] allows model-independent extraction with more parameters; this would increase the uncertainty but provide a more robust result. The dipole assumption may introduce bias if the true form factor deviates from this form.

d. CC DIS analysis. The CC DIS y -leverage analysis (Phase 3) uses ideal Fisher information with no de-

tector smearing or background. A full treatment would require (x, y, Q^2) response matrices and misidentified NC backgrounds.

e. Radiative corrections. QED radiative corrections modify the effective Q^2 and y distributions at the few-percent level. For the elastic channel, the corrections are $\mathcal{O}(\alpha/\pi) \sim 0.2\%$ and negligible. For the CC DIS analysis, radiative effects can be more substantial (several percent) due to initial-state radiation shifting the effective beam energy. The sub-percent xF_3 precision claimed in Table V is *statistical only*; a full treatment would require radiative corrections unfolded with high-fidelity Monte Carlo, which could degrade the precision to the few-percent level. This is comparable to the NuTeV/CHORUS systematics and represents a significant caveat for the DIS analysis.

f. Path forward. The key experimental challenge is background rejection. Our analysis identifies 10^{-7} suppression as the target for a competitive M_A measurement ($\delta M_A \approx 0.14 \text{ GeV}$). This is three orders of magnitude beyond current projections. Achieving this requires: (1) multi-layer forward charged-particle veto with $> 99.9\%$ rejection per layer, (2) ZDC timing and position cuts to reject non-elastic topologies, and (3) machine-learning algorithms trained on PYTHIA/GEANT4 samples to discriminate CC elastic from photoproduction. With these improvements, the EIC could achieve world-leading precision on the nucleon axial form factor using a clean, nuclear-effect-free probe.

IX. CONCLUSIONS

We have demonstrated that the Electron-Ion Collider has the statistical reach to make significant contributions to neutrino physics through charged-current electron-proton scattering.

Using the Fisher information formalism with the inputs in Tables I–II, we present both the Cramér–Rao statistical floor (ideal) and a first-order realistic projection incorporating ZDC acceptance, Q^2 smearing, background noise, and systematic uncertainties (Table IV):

1. **Helicity filtering** provides clean CC signal extraction using RH electron data as an *in situ* EM background template, yielding $S/B \approx 3 \times 10^{-4}$ after forward veto cuts and $\sim 2,200$ CC events from 500 fb^{-1} (Fig. 3).
2. **The elastic CC cross section shape** yields a Cramér–Rao floor of $\delta M_A = 0.032 \text{ GeV}$ (3.2%). With realistic detector effects, this degrades to $\delta M_A \gg 1 \text{ GeV}$, dominated by background noise from the helicity subtraction ($S/B \approx 3 \times 10^{-4}$, reducing the effective Fisher information by $\sim 6,700\times$). Achieving competitive sensitivity ($\delta M_A \approx 0.14 \text{ GeV}$) would require background suppression of $\sim 10^{-7}$ —three orders of magnitude beyond current projections (Fig. 5, Table IV).
3. **The CC DIS y -distribution** separates $F_2^{W^-}$ and $xF_3^{W^-}$ with sub-percent statistical precision for $x > 0.05$, providing the first measurement of xF_3 on a free proton (Fig. 6). This measurement does not suffer from the leading-neutron photoproduction background that limits the elastic channel, making it the most promising near-term electroweak physics goal at the EIC.

The key advantage of the EIC is the *free proton target*, which eliminates the nuclear model uncertainties that dominate current M_A and xF_3 extractions. If sufficient background suppression ($\sim 10^{-7}$) can be achieved, a measurement of M_A at the 14% level on hydrogen would provide qualitatively different information from the $\pm 0.17 \text{ GeV}$ MiniBooNE measurement on carbon, as it directly constrains the nucleon-level form factor without nuclear corrections.

The severely background-limited nature of the elastic channel measurement identifies a critical challenge: current projections (10^{-4} suppression) yield an unfeasible $\delta M_A \approx 4 \text{ GeV}$. Dedicated R&D on background rejection strategies (improved forward tracking, neutral particle identification, machine-learning event classification) is essential. The elastic channel remains an important long-term goal: the statistical floor of $\delta M_A = 0.032 \text{ GeV}$ demonstrates that the fundamental physics reach exists if backgrounds can be controlled. The nuclear target program (Sec. VIII C) represents a further extension that could directly map the A -dependence of neutrino cross sections and definitively resolve the M_A anomaly.

ACKNOWLEDGMENTS

[Acknowledgments to be added.]

Appendix A: Dirac trace technique

The squared matrix element $|\mathcal{M}|^2$, summed over final spins and averaged over initial spins, is computed using:

$$\sum_{\text{spins}} |\bar{u}(p') \Gamma u(p)|^2 = \text{Tr}[(\not{p}' + m') \Gamma (\not{p} + m) \bar{\Gamma}], \quad (\text{A1})$$

where $\bar{\Gamma} = \gamma^0 \Gamma^\dagger \gamma^0$. For the CC elastic process:

$$|\mathcal{M}|^2 = \frac{G_F^2 |V_{ud}|^2}{2} L_{\mu\nu} H^{\mu\nu}, \quad (\text{A2})$$

with the leptonic tensor:

$$L^{\mu\nu} = \text{Tr}[\not{k}' \gamma^\mu (1 - \gamma_5) \not{k} (1 + \gamma_5) \gamma^\nu], \quad (\text{A3})$$

and the hadronic tensor (target spin four-vector s):

$$H^{\mu\nu} = \text{Tr}\left[(\not{P}' + M_n) \Gamma^\mu (\not{P} + M_p) \frac{1 + \gamma_5 \not{s}}{2} \bar{\Gamma}^\nu\right]. \quad (\text{A4})$$

In our implementation, each γ^μ is a 4×4 complex matrix in the Dirac representation, and the trace is computed numerically.

a. Spin four-vector. For longitudinal polarization of a proton with four-momentum $P = (E, 0, 0, |\vec{p}|)$ moving along the z -axis, the spin four-vector is:

$$s^\mu = \frac{1}{M_p} (|\vec{p}|, 0, 0, E), \quad (\text{A5})$$

which satisfies $s \cdot P = 0$ and $s^2 = -1$. For the proton at rest ($|\vec{p}| = 0$), this reduces to $s^\mu = (0, 0, 0, 1)$ (spin along $+z$). The orthogonality condition $s \cdot P = 0$ is verified numerically at each Q^2 point.

b. Mass treatment. In the hadronic tensor, we use the physical proton mass M_p for the initial state and neutron mass M_n for the final state. For kinematic quantities (e.g., $\tau = Q^2/4M^2$), we use the average nucleon mass $M = (M_p + M_n)/2 = 0.939 \text{ GeV}$. The mass difference $(M_n - M_p)/M \approx 0.14\%$ has negligible impact on the extracted M_A .

c. Pseudoscalar form factor. The hadronic vertex Γ^μ includes all four form factors: F_1 , F_2 , F_A , and F_P . Although F_P is suppressed by $m_\ell^2/M^2 \sim 10^{-7}$ for electrons, we include it via the PCAC relation (Eq. 10) to ensure completeness. Its contribution to both the unpolarized cross section and A_{UL} is verified to be $< 10^{-6}$ relative.

This is verified against the Llewellyn Smith formula to $d\sigma_{\text{trace}}/d\sigma_{\text{LS}} = 1.0000$ at all Q^2 . For the spin-dependent terms, we verify $A_{UL}(Q^2 \rightarrow 0) \rightarrow 1$ (the low- Q^2 limit where the axial contribution dominates) and compare against the analytical asymmetry from Ref. [36], finding agreement to $< 0.1\%$ across the full Q^2 range.

Appendix B: Toy PDF parameterization

For the CC DIS analysis, we use analytical PDFs at a fixed scale $Q^2 \sim 10 \text{ GeV}^2$:

$$x u_v(x) = 3.0 x^{0.5} (1-x)^{3.0} (1+3\sqrt{x}), \quad (\text{B1})$$

$$x d_v(x) = 1.0 x^{0.5} (1-x)^{4.0} (1+5\sqrt{x}), \quad (\text{B2})$$

$$x \bar{q}(x) = 0.4 x^{-0.2} (1-x)^{7.0}, \quad (\text{B3})$$

$$x c(x) = 0.15 (1-x)^{8.0}, \quad (\text{B4})$$

with $\bar{u} = \bar{d} = \bar{q}$ and $s = \bar{s} = 0.5\bar{q}$. These capture the qualitative features of modern PDF sets: u_v peaks at $x \approx 0.2$ with integral 2, d_v peaks at $x \approx 0.15$ with integral 1, the sea rises at small x , and charm is suppressed. DGLAP evolution is not included. For a definitive analysis, LHAPDF [35] with a modern PDF set should be used; the toy parameterization is sufficient for demonstrating the y -leverage method and estimating the statistical precision.

-
- [1] B. Abi *et al.* (DUNE Collaboration), “Deep Underground Neutrino Experiment (DUNE), Far Detector Technical Design Report, Volume II: DUNE Physics,” arXiv:2002.03005 [hep-ex].
- [2] J. A. Formaggio and G. P. Zeller, “From eV to EeV: Neutrino cross sections across energy scales,” *Rev. Mod. Phys.* **84**, 1307 (2012), arXiv:1305.7513.
- [3] S. Navas *et al.* (Particle Data Group), “Review of Particle Physics,” *Phys. Rev. D* **110**, 030001 (2024).
- [4] V. Bernard, L. Elouadrhiri, and U.-G. Meißner, “Axial structure of the nucleon,” *J. Phys. G* **28**, R1 (2002), arXiv:hep-ph/0107088.
- [5] A. A. Aguilar-Arevalo *et al.* (MiniBooNE Collaboration), “First measurement of the muon neutrino charged current quasielastic double differential cross section,” *Phys. Rev. D* **81**, 092005 (2010), arXiv:1002.2680.
- [6] D. Ruterbories *et al.* (MINERvA Collaboration), “Simultaneous measurement of muon neutrino quasielastic-like cross sections on CH, C, water, Fe, and Pb as a function of muon kinematics at MINERvA,” *Nature* **614**, 48 (2023).
- [7] M. Martini, M. Ericson, G. Chanfray, and J. Marteau, “Unified approach for nucleon knock-out and coherent and incoherent pion production in neutrino interactions with nuclei,” *Phys. Rev. C* **80**, 065501 (2009), arXiv:0910.2622.
- [8] J. Nieves, I. Ruiz Simo, and M. J. Vicente Vacas, “Inclusive charged-current neutrino-nucleus reactions,” *Phys. Rev. C* **83**, 045501 (2011), arXiv:1102.2777.
- [9] R. Abdul Khalek *et al.*, “Science Requirements and Detector Concepts for the Electron-Ion Collider: EIC Yellow Report,” *Nucl. Phys. A* **1026**, 122447 (2022), arXiv:2103.05419.
- [10] T. Klest, “Charged-current elastic neutrino cross section measurement at the Electron-Ion Collider,” arXiv:2511.02049 [hep-ph] (2025).
- [11] C. H. Llewellyn Smith, “Neutrino reactions at accelerator energies,” *Phys. Rep.* **3**, 261 (1972).
- [12] J. Arrington, C. D. Roberts, and J. M. Zanotti, “Nucleon electromagnetic form factors,” *J. Phys. G* **34**, S23 (2007), arXiv:nucl-th/0611050.
- [13] M. Tzanov *et al.* (NuTeV Collaboration), “Precise measurement of neutrino and anti-neutrino differential cross sections,” *Phys. Rev. D* **74**, 012008 (2006), arXiv:hep-ex/0509010.
- [14] G. Onengut *et al.* (CHORUS Collaboration), “Measurement of nucleon structure functions in neutrino scattering,” *Phys. Lett. B* **632**, 65 (2006), arXiv:hep-ex/0503033.
- [15] G. Cowan, *Statistical Data Analysis* (Oxford University Press, Oxford, 1998).
- [16] R. A. Smith and E. J. Moniz, “Neutrino reactions on nuclear targets,” *Nucl. Phys. B* **43**, 605 (1972); **101**, 547(E) (1975).
- [17] A. Buckley *et al.*, “LHAPDF6: parton density access in the LHC precision era,” *Eur. Phys. J. C* **75**, 132 (2015), arXiv:1412.7420.
- [18] F. Akbar, M. Rafi Alam, M. Sajjad Athar, and S. K. Singh, “Quasielastic production of polarized hyperons in antineutrino-nucleon reactions,” *Phys. Rev. D* **96**, 093001 (2017), arXiv:1707.02253.
- [19] B. Abi *et al.* (DUNE Collaboration), “Deep Underground Neutrino Experiment (DUNE), Far Detector Technical Design Report, Volume II: DUNE Physics,” arXiv:2002.03005 [hep-ex].
- [20] J. A. Formaggio and G. P. Zeller, “From eV to EeV: Neutrino cross sections across energy scales,” *Rev. Mod. Phys.* **84**, 1307 (2012), arXiv:1305.7513.
- [21] S. Navas *et al.* (Particle Data Group), “Review of Particle Physics,” *Phys. Rev. D* **110**, 030001 (2024).
- [22] V. Bernard, L. Elouadrhiri, and U.-G. Meißner, “Axial structure of the nucleon,” *J. Phys. G* **28**, R1 (2002), arXiv:hep-ph/0107088.

- [23] A. A. Aguilar-Arevalo *et al.* (MiniBooNE Collaboration), “First measurement of the muon neutrino charged current quasielastic double differential cross section,” *Phys. Rev. D* **81**, 092005 (2010), arXiv:1002.2680.
- [24] D. Ruterbories *et al.* (MINERvA Collaboration), “Simultaneous measurement of muon neutrino quasielastic-like cross sections on CH, C, water, Fe, and Pb as a function of muon kinematics at MINERvA,” *Nature* **614**, 48 (2023).
- [25] M. Martini, M. Ericson, G. Chanfray, and J. Marteau, “Unified approach for nucleon knock-out and coherent and incoherent pion production in neutrino interactions with nuclei,” *Phys. Rev. C* **80**, 065501 (2009), arXiv:0910.2622.
- [26] J. Nieves, I. Ruiz Simo, and M. J. Vicente Vacas, “Inclusive charged-current neutrino-nucleus reactions,” *Phys. Rev. C* **83**, 045501 (2011), arXiv:1102.2777.
- [27] R. Abdul Khalek *et al.*, “Science Requirements and Detector Concepts for the Electron-Ion Collider: EIC Yellow Report,” *Nucl. Phys. A* **1026**, 122447 (2022), arXiv:2103.05419.
- [28] T. Klest, “Charged-current elastic neutrino cross section measurement at the Electron-Ion Collider,” arXiv:2511.02049 [hep-ph] (2025).
- [29] C. H. Llewellyn Smith, “Neutrino reactions at accelerator energies,” *Phys. Rep.* **3**, 261 (1972).
- [30] J. Arrington, C. D. Roberts, and J. M. Zanotti, “Nucleon electromagnetic form factors,” *J. Phys. G* **34**, S23 (2007), arXiv:nucl-th/0611050.
- [31] M. Tzanov *et al.* (NuTeV Collaboration), “Precise measurement of neutrino and anti-neutrino differential cross sections,” *Phys. Rev. D* **74**, 012008 (2006), arXiv:hep-ex/0509010.
- [32] G. Onengut *et al.* (CHORUS Collaboration), “Measurement of nucleon structure functions in neutrino scattering,” *Phys. Lett. B* **632**, 65 (2006), arXiv:hep-ex/0503033.
- [33] G. Cowan, *Statistical Data Analysis* (Oxford University Press, Oxford, 1998).
- [34] R. A. Smith and E. J. Moniz, “Neutrino reactions on nuclear targets,” *Nucl. Phys. B* **43**, 605 (1972); **101**, 547(E) (1975).
- [35] A. Buckley *et al.*, “LHAPDF6: parton density access in the LHC precision era,” *Eur. Phys. J. C* **75**, 132 (2015), arXiv:1412.7420.
- [36] F. Akbar, M. Rafi Alam, M. Sajjad Athar, and S. K. Singh, “Quasielastic production of polarized hyperons in antineutrino-nucleon reactions,” *Phys. Rev. D* **96**, 093001 (2017), arXiv:1707.02253.